

Novel Movable Typing for Personalized Vein-Chips in Large Scale: Recapitulate Patient-Specific Virchow's Triad and its Contribution to Cerebral Venous Sinus Thrombosis

Yunduo Charles Zhao, Yingqi Zhang, Zihao Wang, Fengtao Jiang, Kiarash Kyanian, San-Seint-Seint Aye, Tianbo Hong, Parham Vatankhah, Arian Nasser, Allan Sun, Laura Moldovan, Qian P. Su, Ann-Na Cho, Yao Wang, Freda Passam, Timothy Ang, and Lining Arnold Ju*

The Vein-Chip recapitulates CVST Virchow's triad and enables systematic characterization of venous thrombogenesis with respect to fibrin formation and platelet aggregation. Distinct from the arterial setting, platelets universally adhere across the entire CVS Vein-Chip independent of stenotic geometry and flow disturbance. Intriguingly, fibrin propagates along with the flow direction, but exclusively deposits to the inner vessel wall. Upon inflammatory endothelial injury, fibrin deposition mirrors to the outer vessel wall, but still not in the lumen. Together, the Vein-Chip promises future applications for personalized thrombotic assessment and monitoring.

intensively studied and modeled,^[2-5] venous thrombosis, particularly in the brain, such as cerebral venous sinus thrombosis (CVST), remains underexplored. The lack of emphasis on integrative research in CVST can partly be attributed to its rarity compared to arterial stroke,^[6] nonspecific signs and symptoms in patients,^[7] and highly heterogeneous cerebral venous sinus (CVS) anatomy,^[8] making clinical diagnoses and monitoring more challenging. Consequently, there are limited animal models and one-size-fits-all

1. Introduction

Cerebral thrombosis and its associated strokes ranks as the second leading cause of death and the primary cause of disability globally.^[1] Unlike arterial thrombosis, which has been

in-vitro systems available to decipher the critical mechanisms underlying CVST, let alone personalized treatments.^[9,10] However, the number of CVST cases causing stroke or permanent disability continues to increase.^[6,9] Particularly, its association with the COVID-19 vaccine-induced immune thrombotic

Y. C. Zhao, Y. Zhang, Z. Wang, F. Jiang, K. Kyanian, S.-S.-S. Aye, T. Hong, P. Vatankhah, A. Nasser, A. Sun, L. Moldovan, Y. Wang, L. A. Ju
School of Biomedical Engineering
The University of Sydney
Darlington, NSW 2008, Australia
E-mail: arnold.ju@sydney.edu.au

Y. C. Zhao, Y. Zhang, F. Jiang, A. Sun, L. Moldovan, L. A. Ju
Charles Perkins Centre
The University of Sydney
Camperdown, NSW 2006, Australia

Y. C. Zhao, Y. Zhang, F. Jiang, L. A. Ju
The University of Sydney Nano Institute (Sydney Nano)
The University of Sydney
Camperdown, NSW 2006, Australia

Z. Wang
School of Aerospace, Mechanical and Mechatronic Engineering
The University of Sydney
Darlington, NSW 2008, Australia

 The ORCID identification number(s) for the author(s) of this article can be found under <https://doi.org/10.1002/adfm.202214179>.

© 2023 The Authors. Advanced Functional Materials published by Wiley-VCH GmbH. This is an open access article under the terms of the Creative Commons Attribution License, which permits use, distribution and reproduction in any medium, provided the original work is properly cited.

DOI: 10.1002/adfm.202214179

A. Sun, L. Moldovan, F. Passam, L. A. Ju
Heart Research Institute
Camperdown, Newtown, NSW 2042, Australia

Q. P. Su
School of Biomedical Engineering
Faculty of Engineering and Information Technology
University of Technology Sydney
Sydney, NSW 2007, Australia

A.-N. Cho
Dementia Research Centre
Macquarie Medical School
Faculty of Medicine Health and Human Sciences
Macquarie University
Macquarie Park, NSW 2109, Australia

F. Passam
Department of Haematology
Royal Prince Alfred Hospital
Camperdown, NSW 2006, Australia

F. Passam
Central Clinical School
Faculty Medicine and Health
The University of Sydney
Camperdown, NSW 2006, Australia

T. Ang
Departments of Interventional Neuroradiology Neurology
Royal Prince Alfred Hospital
Camperdown, NSW 2006, Australia

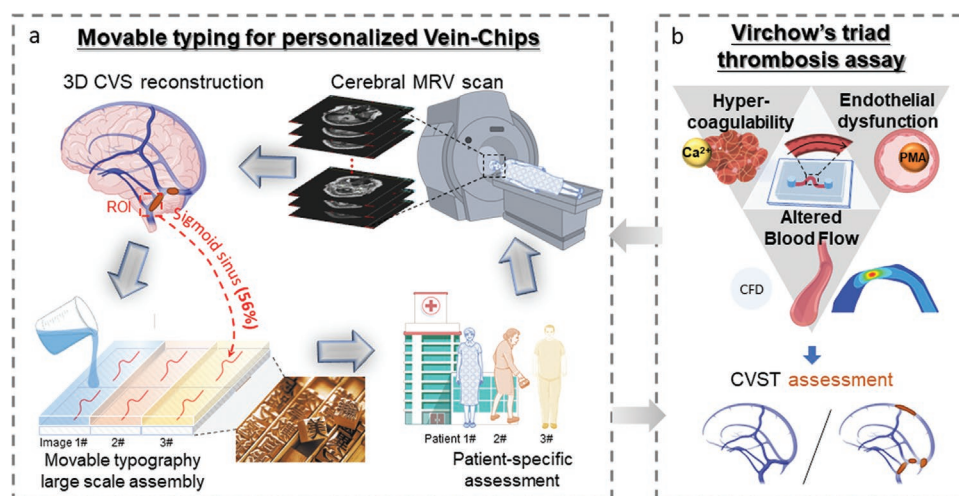


Figure 1. Concept of movable typed Vein-Chip platform to recapitulate patient-specific Virchow's triad and thrombotic assessment. a) Schematic illustration of the design and microfabrication of cerebral venous sinus (CVS)-on-chip models. The CVS geometries were first numerically reconstructed from a high-contrast magnetic resonance venography (MRV) image from a CVST patient. The target vessel of interest is one segmentation of the sigmoid sinus representing > 56% of all CVST cases.^[31] We then translated it into a Vein-Chip by 3D stereolithography (see Experimental Section). Note that multiple chip molds were assembled to a larger plate for mass production to reduce production time and cost. In an ideal future, our scaled-up, low-cost, and fast-turnover biofabrication capability by movable typing would enable large-scale personalized thrombotic assessment by targeting multiple vascular segments for one patient, applying to a number of at-risk patients and long-term monitoring at multiple time points. b) The endothelialized Vein-Chips evaluate patient-specific Virchow's triad: hemodynamics, endothelial dysfunction, and hypercoagulability, promising future personalized thrombotic assessment in a clinic.

thrombocytopenia or VITT has garnered more attention in recent years.^[11,12]

Conventional diagnostic tools for assessing cerebrovascular disease, such as magnetic resonance imaging (MRI) and computed tomography (CT) scans, are non-invasive imaging modalities widely available for assessing stroke patients.⁵⁷ However, identifying vulnerable patients by degree of stenosis is a suboptimal over-simplification. More advanced techniques with higher sensitivity have been proposed to better qualify the recurrent risk of CVST patients.^[14] Unfortunately, these techniques have not yet been well validated or readily accessible even in metropolitan tertiary centers. For the CVS vasculature, the spatial resolution of MRI and CT technologies limits our ability to assess intravascular hemodynamics and coagulability.^[15] To obtain high-resolution CVS anatomies, non-invasive magnetic resonance venography (MRV) harnesses intravenous contrast dye to visualize the veins,^[16] making MRV the golden standard for diagnosing CVST and other non-acute thrombosis and related stroke^[15] (Figure 1a).

Although it has been known for over a century that thrombosis is triggered by Virchow's triad^[17] (Figure 1b), current diagnostic and surveillance strategies poorly capture the complex interplay among the vessel wall morphology, hemodynamic flow disturbance, and coagulability,^[6] let alone efficiently predict an individual's response to antithrombotic medication.^[18] Despite significant advances in diagnostic imaging and medical therapy, no standardized testing can identify which individuals are at high risk of a thrombotic event,^[19] due to large variability from one to another based on personal anatomical, genetic, and environmental factors.^[6,8,9,20] There also remains a significant percentage of patients who do not have a recognized etiology of their CVST and experience recurrent thrombotic events.^[21–23] Blood coagulation tests and platelet function analyses have been undertaken to predict thrombotic risk without vessel wall.^[3,24,25]

However, such methodologies are reliant on labor-intensive testing, bulky and costly equipment, and specialist interpretation^[14,26] – all of which are poorly available in regional and rural health settings. Currently, there is no personalized and affordable point-of-care testing available that allows for tailored risk stratification as well as long-term monitoring.^[27–29]

To address this challenge, we developed a CVS-on-a-chip (Vein-Chip)—a microfluidic model mimicking the venous geometry of a CVST patient, where living endothelial tissue and whole blood flow provide the incorporation and dissection of Virchow's triad. Specifically, we reconstructed the CVS vasculature from high-contrast MRV images and translated it into a Vein-Chip by 3D stereolithography (Figure 1). Notably, to produce the Vein-Chips in large quantities and rapidly with various vascular segmentation, we were inspired by the Chinese Type—the ancient system and technology of printing and typography that uses movable components to reproduce the elements of a document (individual alphanumeric characters or punctuation marks) usually on the medium of paper^[30] (Figure 1a). By further combining hydrodynamic shear mapping, endothelialization, and coagulability modulation, we systematically revealed the relative contribution of Virchow's triad on CVST Vein-Chips. The Vein-Chip platform recapitulates CVST Virchow's triad and enables systematic characterization of venous thrombogenesis with respect to fibrin formation and platelet aggregation.

2. Results

2.1. Cerebral Venous Sinus Geometry Reconstruction and Vein-Chip Fabrication

We initially sought to determine the anatomy of a typical human vein in the brain, which would provide a geometric design for

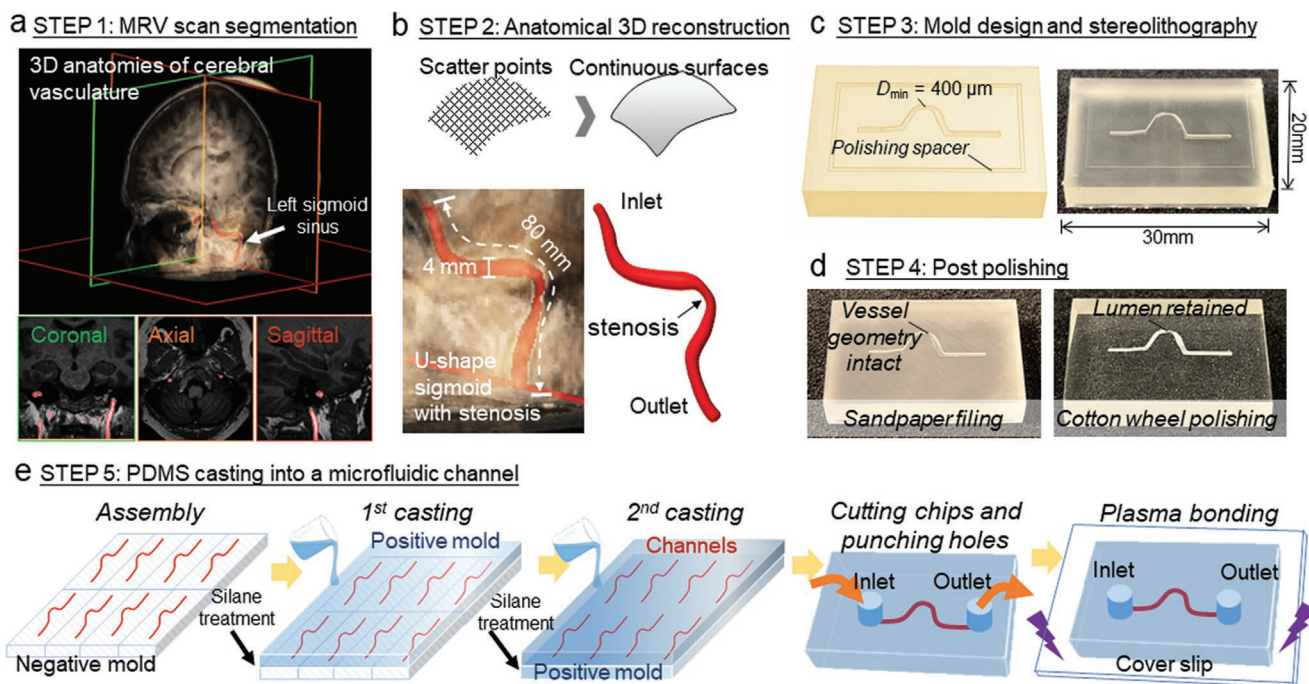


Figure 2. Patient's clinical image derived Vein-Chip design and movable typing for large-scale fabrication. a) The MRV scan before the patient was confirmed with CVST. The left sigmoid sinus segmentation with a stenotic region was selected to recapitulate CVST on a chip. b) 3D reconstruction from the vascular anatomy. The MRV image of the target vessel was first reconstructed into STL formatted facades via the DICOM viewer. Such facades were then converted into curvature-based continuous surfaces using the ANSYS SpaceClaim. c) Translating the vascular anatomy to a positive mold by 3D stereolithography. d) Polishing and production of a smooth surface and intact vascular surface in two steps. e) Mass production by two PDMS casting procedures. First, the negative Vein-molds were assembled to a large plate and cast as a positive Vein-mold. Then the second PDMS-to-PDMS casting was performed, followed by cutting into single microfluidic chips with negative vessel geometries. Each chip was then punched with two holes as inlet and outlet, and plasma-bonded onto a coverslip to form an enclosed channel for endothelialization.

a microfluidic device. In the first step, we analyzed the MRV scan of a 70-year-old female patient (Figure 2a) and segmented the sigmoid sinuses with a longitudinal length of 80 mm and a luminal diameter of 4 mm. Such location was reported to contribute > 56% of the CVST cases.^[31] We then took the left segmentation from the patient's sigmoid sinus for our microfluidic design as a proof of concept.

In the second step, with our customized surface smoothing algorithm^[32] (see Experimental Section; Figure 2b), we numerically reconstructed the 3D anatomy of this U-shape sigmoid sinus with a stenotic region. To translate this vein geometry to a microfluidic device as a Vein-Chip, we scaled down the luminal diameter by a factor of 0.15 to a minimum diameter, $D_{\min} = 400 \mu\text{m}$, suitable for standard stereolithography (SLA) 3D printing (Figure 2c).

In the third step, the vessel geometry was subtracted from a block, and 3D printed to form a negative mold (Figure 2c). A supporting scaffold was used with optimized geometry settings to achieve z-axis accuracy at $\pm 5 \mu\text{m}$ (Figure S1a, Supporting Information). Due to the nature of the SLA printing technique, some extra supports were allocated at the edge of the chip to prevent surface distortion.

In the fourth step, the mold surface was further filled with sandpapers and polished by a cotton wheel (Figure 2d). Mirror-like smoothness was achieved (Figure S1b, Supporting Information). To avoid damaging the microfluidic geometry, a rectangular trench was designed to better control polishing depth

(Figure 2c). As a result, the vessel geometry was intact relative to the original microfluidic design (Figure 2d, right).

In the fifth step, we assembled the 3D-printed negative Vein-molds into a large plate, followed by silane treatment for mass production using 3D soft-lithography in one go (Figure 2e). Two PDMS casting procedures were used to make the positive mold (Figure S1c, Supporting Information) and the Vein-Chips. After punching the inlet and outlet, the Vein-Chip was then plasma bonded to a coverslip to form an enclosed microfluidic channel (Figure 2e; see Experimental Section). The above methods of producing precise and sophisticated Vein-Chip were optimized from multiple printing designs, materials selection, and polishing procedures (Table 1; Figure S1, Supporting Information).

2.2. Fluid Flow Characterization for Distinct Vascular Zones on a Vein-Chip

To characterize fluid flow profiles and distinct shear zones, computational fluid dynamics (CFD) analyses were performed as described previously^[25,35,36] to map shear rate distributions and velocity streamlines at both the original MRV scale (Figure 3a,b) and microfluidic scale (Figure 3c–e). At a physiological venous bulk shear rate $\dot{\gamma}_0 = 150 \text{ s}^{-1}$, the wall shear rate distributions around the stenosis are very similar between the MRV vessel geometry (Figure 3a) and the miniaturized Vein-Chip model (Figure 3c). The wall shear rates in pre- and

Table 1. Material selection for Vein-Chip fabrication steps 3–5.

Fabrication step 3: 3D printed negative mold					
Materials	Polishing time	Surface finish	Printing Temperature	Printing Time	IPA Washing Time
Flex resin	N/A	surface damage	Room temperature	240 min	20 min
Rigid resin	> 20 min	Good	Room temperature	240 min	20 min
Clear resin	2 min	Specular	Room temperature	240 min	20 min
Fabrication step 4: positive mold casting					
Materials	Demolding	Thermal Deformation	Curing Temperature	Curing Time	Curing Environment
Photoresist SU8	Slow	Bent	Room temperature	120 min	Clean room
Loctite AA 358	Broken	Flat	Room temperature	10 min	PC1 lab
Flex resin	Fast	Bent	60 °C	60 min	Clean room
PDMS	Fast	Flat	80 °C	120 min	PC1 lab
Fabrication step 5: final channel casting					
Materials	Transparency	Biocompatibility	Curing Temperature	Curing Time	Curing Environment
Photoresist SU8	Dark transparent	Biocompatible	Room temperature	120 min	Clean room
Clear resin	yellowish transparent	Non-Biocompatible	Room temperature	30 min	Clean room
PDMS	optically transparent	Biocompatible	80 °C	120 min	PC1 lab

The fabrication steps 3 to 5 were optimized from multiple trials to meet the following requirements: i) The negative Vein-mold shall be polishable with a smooth surface finish; ii) the post polishing process shall not damage the details of the microfluidic geometry; iii) the material of the positive Vein-mold shall retain high spatial resolution after casting, and it shall be strong enough for the following casting procedure; iv) the material of the Vein-Chip shall be transparent for fluorescent imaging and v) the Vein-Chip shall be biocompatible for endothelial cells culturing. To this end, three materials, rigid resin, clear resin, and flex resin, were compared for the negative molding—step 3. After carefully evaluating the polishing time and surface finish quality, the clear resin was selected due to its greater product quality and time efficiency (Figure S2, Supporting Information). In step 4, various materials were compared for the positive mold fabrication, including the flex resin, Loctite 385 UV-cured epoxy, SU8 photoresist, and PDMS. The flex resin and SU8 mold significantly deformed after being heated up from room temperature to 80 °C, making them less compatible for the next steps. The trials using Loctite 385 also failed because peeling off from the negative mold in step 3 would likely introduce mechanical damages due to its high fragility. Eventually, the PDMS was selected to produce the positive Vein-mold as it can easily be peeled off from the negative mold after silane treatment with minimum thermal deformation.^[33] In step 5, three transparent materials, SU8, clear resin and PDMS were tested. SU8 and UV-cured resins were excluded because of low transparency and limited biocompatibility derived from non-uniform photo-crosslinking, respectively.^[34] Thus, PDMS was selected to produce the final microfluidic channels due to its superiority in thermoplasticity, biocompatibility, and transparency combination.

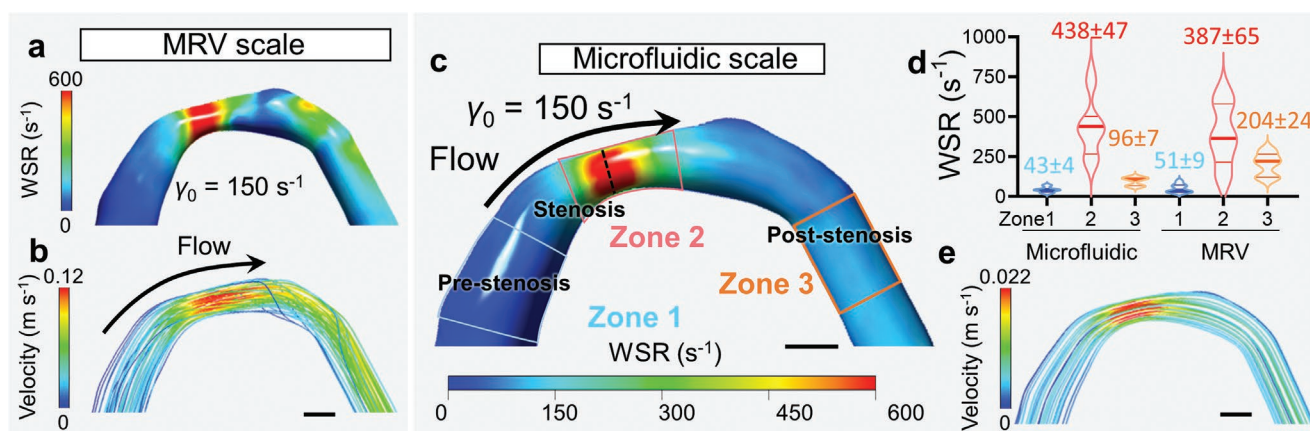


Figure 3. Flow profile characterization of the MRV vessel geometry and Vein-Chip model. CFD analyses showing the wall shear rate (WSR) distribution at the top surface a) and velocity streamlines at the interstitial volume b) of the MRV vessel geometry. To achieve physiological venous bulk shear rate $\gamma_0 = 150 \text{ s}^{-1}$, an input flow of 1.08 ml min^{-1} was used as the boundary condition for the simulation. c) CFD analyses showing the WSR contour at the top surface of the microfluidic scale Vein-Chip. Note that three WSR zones were identified. d) WSR distribution for the microfluidic and MRV scale at each zone. Typical shear rates in the non-stenotic sections of the 3D vessel were in the range of $15\text{--}150 \text{ s}^{-1}$. Because of the 44% stenosis, higher wall shear rates were displayed in zone 2, with mean shear rates higher than 380 s^{-1} for both scales. e) CFD velocity streamlines at the interstitial volume of the microfluidic scale vessel geometry. Similar flow profiles in three distinct shear zones were demonstrated with wall shear rates and velocity. Scale bars (a) and (b), 3 mm. Scale bars (c) and (e), $400 \mu\text{m}$.

post-stenotic zones are 43 ± 4 and $96 \pm 7 \text{ s}^{-1}$, respectively (zone 1 and 3, Figure 3c). When approaching the stenosis ($\approx 44\%$ narrowing), they rapidly exceeded $439 \pm 47 \text{ s}^{-1}$ (zone 2, Figure 3c) for both scales. The average shear rate of zone 2 is the highest, more than ten times greater than zone 1, and four times greater than zone 3 (Figure 3d). Although the velocity magnitude varied between the two scales, similar flow velocity patterns were observed in the three distinct shear zones (Figure 3b,e). Thereby, the microfluidic scaledown from the MRV geometry was justified.

2.3. Vascular Inflammation and Endothelial Phenotypic Changes

To fully biofunctionalize the Vein-Chip and mimic vessel wall injuries, human umbilical endothelial cells (HUVECs) were seeded in the microfluidic channels (see Experimental Section). The endothelial cells were grown and proliferated to form a confluent monolayer after incubation in the chip for 1 day (Figure 4a) under static conditions. Confocal microscopy revealed that HUVECs were successfully attached and aligned as endothelium across the entire microfluidic channel

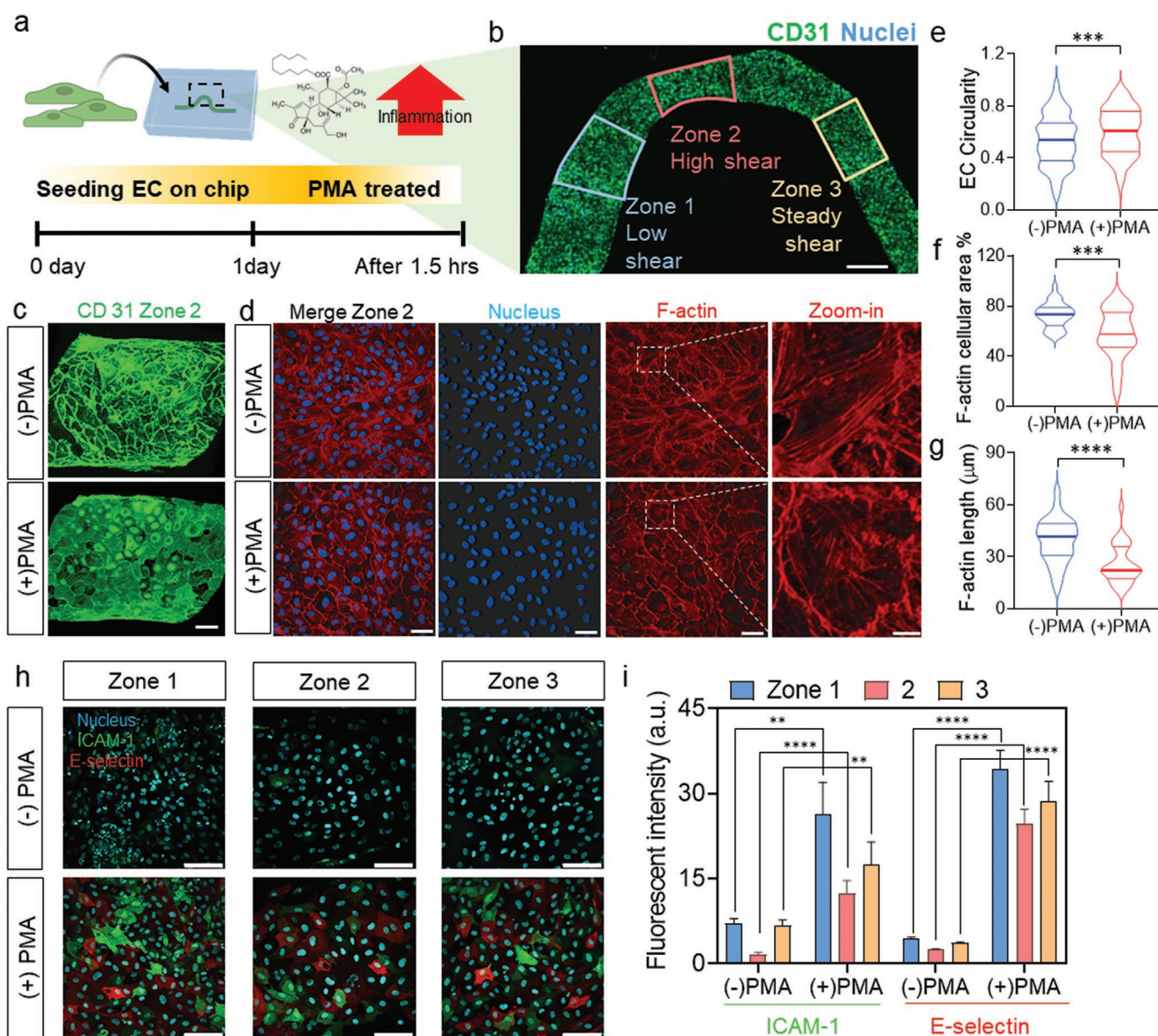


Figure 4. Vein-Chip endothelialization and proinflammatory injury. a) HUVECs were seeded in a bare Vein-Chip for one day, then treated with PMA for 1.5 h to model the inflammatory state. b) Confocal microscopy and image stitching of functional endothelium lined inside a microfluidic channel. Anti-CD31 (green) and nuclear stain (cyan) showed endothelialization at the bottom surface of the entire microfluidic channel. Scale bar = 400 μm ; c,d) Representative immunostaining images of CD31 (c; Scale bar = 80 μm) and F-actin (d; scale bar = 50 μm) expression at the endothelial junctions and cell bodies to indicate the healthy (upper) and injured (lower) morphology status in the absence (-) or presence (+) of PMA stimulation. Quantification of EC circularity (e), F-actin positive area percentage (f), F-actin stress fiber length (g). Data was shown as violin plots of $n \geq 30$ cells evaluated in duplicate. h) Representative immunostaining images of ICAM-1 (green) and E-selectin (red) expression at zone 1, 2, and 3 in the absence (-) or presence (+) of PMA stimulation. Scale bar = 50 μm . i) The fluorescence intensity of ICAM-1 and E-selectin at three shear zones in the absence (-) or presence (+) of PMA stimulation. ** = $p < 0.005$, *** = $p < 0.001$, **** = $p < 0.0001$, assessed by unpaired, two-tailed Student's *t*-test.

(Figure 4b). The CD31 expression at the integral endothelial junction demonstrated that our Vein-Chips were grossly functionalized in a healthy state (Figure 4b,c).

Several studies have suggested that the vessel wall injury can lead to endothelial activation, barrier disruption, and increased venous thrombosis *in vivo*.^[37,38] Therefore, we stimulated endothelialized Vein-Chips with short-term exposure to phorbol-12-myristate-13-acetate (PMA) to model inflammatory conditions (Figure 4a). Compared to the non-treated condition (Figure 4c,d, upper), the inflamed endothelial cells inside the microfluidics displayed more circular morphology, reduced CD31 expression at the junction (Figure 4c, lower), and F-actin expression (Figure 4d, lower) after 150 ng mL⁻¹ PMA treatment for 1.5 h. The circularity of endothelial cells was significantly increased to 0.60 ± 0.01 compared to 0.53 ± 0.01 of the non-treated groups (Figure 4e). In addition, the percentage of F-actin-positive cell area decreased from 73 ± 2% to 57 ± 4% for endothelial cells upon PMA injury (Figure 4f). Similarly, the length of F-actin stress fiber significantly decreased from 39 ± 2 to 26 ± 2 μm as a result of PMA stimulation (Figure 4g). In order to verify the impact of endothelial injury, the expression levels of two inflammatory markers, intercellular adhesion molecule-1 (ICAM-1) and E-selectin, were assessed under both non-treated and PMA-treated conditions across three shear zones (Figure 4h). Our findings showed that compared to the non-treated conditions, the ICAM-1 intensity on the endothelial cells at zones 1, 2, and 3 increased by 3.7, 7.8, and 2.6 folds, respectively, while the E-selectin intensity increased by 7.6, 9.7, and 7.7 folds, respectively (Figure 4i). The results mimicked vascular injury and characterized the changes of the endothelial phenotypes on a CVS Vein-Chip.

2.4. Whole Blood Perfusion in the Vein-Chip to Assess Thrombotic Response

In order to model venous thrombosis, citrated human blood was recalcified and then perfused through the endothelialized Vein-Chips at physiological venous bulk shear rate $\gamma_0 = 150 \text{ s}^{-1}$ for 10 min (Figure 5a). To quantify thrombotic response, we used confocal microscopy to visualize real-time immunostaining of developing platelet aggregates (Figure 5b, white) and fibrin formation (Figure 5b, magenta). To further modulate thrombosis, we challenged the Vein-Chip to higher CaCl₂ doses above physiological conditions from 1 to 4 mM (Figure 5b–d).^[39] Notably, at physiological calcium doses of 1–2 mM, there was little fibrin deposited to the endothelium at any time (Figure 5c, black and orange), while the higher recalcification dose resulted in rapid and highly dynamic fibrin formation with excessive growth at $t = 5$ to 8 min (Figure 5b). Interestingly, we found that fibrin was mostly deposited where platelet aggregation existed (Figure 5d). Their growth seemed triggered by platelet adhesion onto the endothelium, consistent with other venous thrombosis models.^[40]

Next, we hypothesized that the stenosis in the middle of the sigmoid sinus could change hemodynamics both upstream and downstream, therefore affecting CVST as observed clinically.^[8,20] To correlate the hemodynamics with thrombosis, we quantified the platelet and fibrin fluorescence intensity across all three shear zones (indicated in Figure 3b). To our surprise, platelet adhesion and aggregation exhibited non-significant differences among three shear zones and under all recalcification doses (Figure 5e). While fibrin initiated from zone 1 and then propagated to zone 3

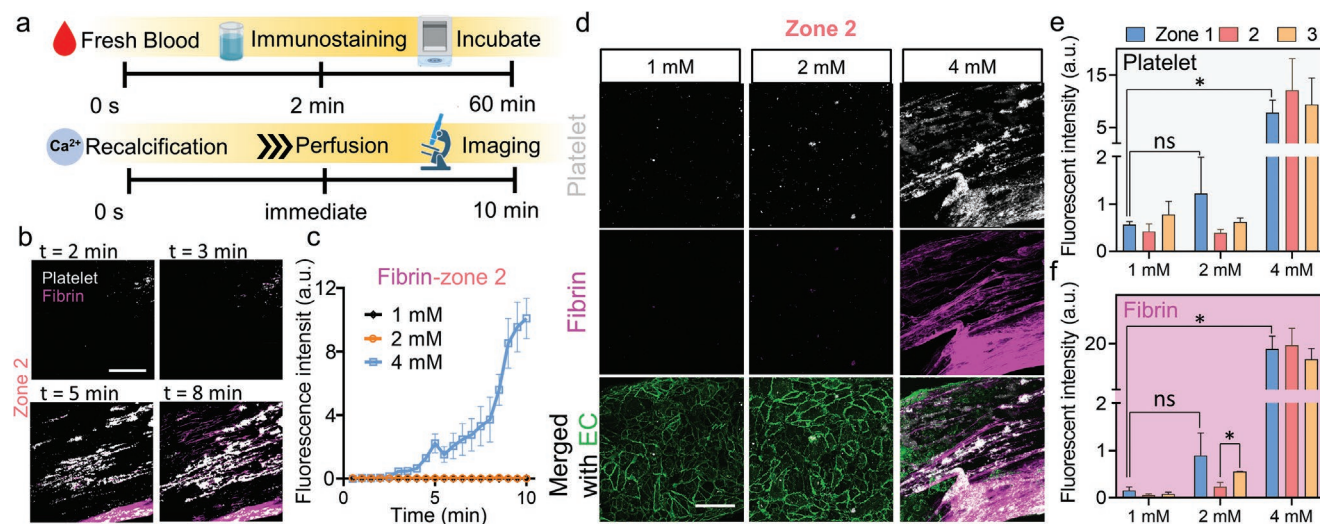


Figure 5. Recalcified whole blood perfusion in the Vein-Chip to assess thrombotic response. a) Citrated whole blood was re-calcified and then perfused for 10 min at a bulk shear rate of 150 s⁻¹ in the Vein-Chips. b) Representative platelet and fibrin signal images at 2, 3, 5, and 8 min marks under 4 mM CaCl₂ dose. The images represent $n = 5$ independent experiments performed in duplicate. c) Time-lapse quantitation of fibrin formation at stenotic zone 2 of a Vein-Chip. Fibrin is seen at the apex of the stenosis for 4 mM CaCl₂ dose, while there is little fibrin formation after 10 min perfusion for 1 and 2 mM recalcification. d) Confocal images of platelet aggregation (Row 1) and fibrin formation (Row 2) were examined at 1 mM (Column 1), 2 mM (Column 2) and 4 mM (Column 3) CaCl₂. Merged platelet and fibrin signals with endothelial cells (Row 3). Platelets (anti-CD41) and fibrin were immunostained by anti-CD41-Atto555 (SZ22) and fibrin with anti-fibrin-Alexa647 (59D8). The flow direction is from left to right. Images represent $n \geq 3$ independent experiments. Scale bar = 50 μm. The fluorescence intensity of platelet aggregation e) and fibrin formation f) after 10 min perfusion at three shear zones and under 1, 2, and 4 mM CaCl₂ doses. Data represents mean ± s.e.m. of $n \geq 3$ independent experiments in duplicate. * = $p < 0.05$, assessed by unpaired, two-tailed Student's *t*-test.

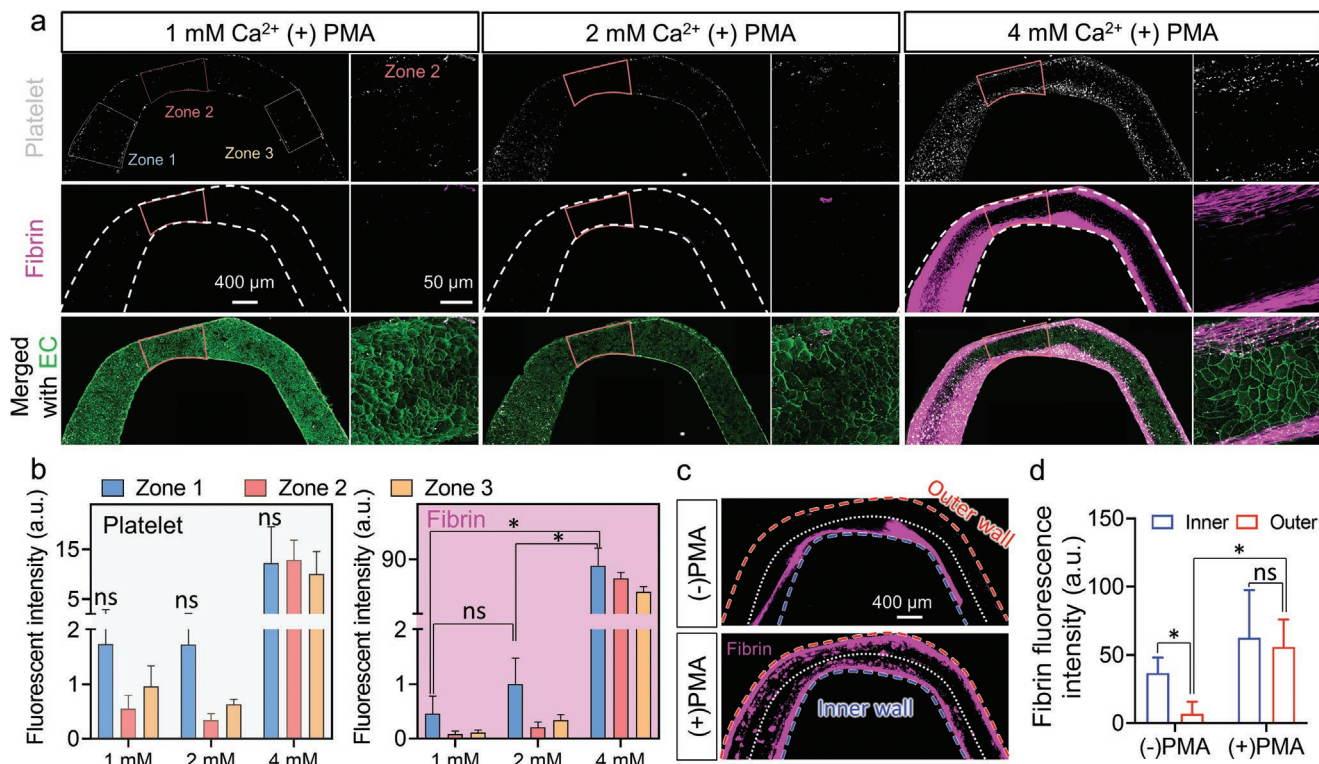


Figure 6. Vessel wall injury effect to thrombotic response in a Vein-Chip. a) 2D confocal stitching images of platelet aggregation (Row 1) and fibrin expression (Row 2) were examined at 1 mM (Column 1), 2 mM (Column 2) and 4 mM (Column 3) CaCl₂ with 50 ng mL⁻¹ PMA treatment. Merged images showed that endothelial conditions for each representative Vein-Chip are good (Row 3). Images represent $n \geq 3$ independent experiments (Scale bars 400 μm). b) Fluorescence intensity quantification for platelet (left) and fibrin (right). c) Representative confocal images of fibrin deposition in the Vein-Chip, non-treated (top) or treated (bottom) with PMA. Note the fibrin was expressed mainly at the inner wall (blue) in non-treated Vein-Chips while observed at both inner and outer walls (red) in PMA-treated Vein-Chips. d) Fluorescence intensity quantification of fibrin deposition at the inner and outer halves of the Vein-Chip. All data presents mean \pm s.e.m. of $n \geq 3$ independent experiments in duplicate. * = $p < 0.05$, assessed by unpaired, two-tailed Student's *t*-test.

in the direction of flow (cf. **Figure 6a**). Similar to platelets, the fibrin level showed non-significant differences among three shear zones (**Figure 5f**). Both platelet aggregation and fibrin formation increased with recalcification doses from 1–4 mM (**Figure 5e,f**). Distinct from the microfluidic studies on arterial thrombosis, our results suggest that the CVST is fibrin-rich and likely independent of biomechanical platelet aggregation as observed at the arterial stenosis and with high shear gradients.^[24,41–43]

2.5. Investigate the Thrombotic Effects of the Endothelial Injury on a Vein-Chip

We further investigated the thrombotic effects of vessel wall injury by stimulating the endothelialized Vein-Chip with 150 ng mL⁻¹ PMA for 1.5 h. Recalcified blood was perfused for 10 min. Similar to non-treated conditions, both platelet aggregation and fibrin formation significantly increased along with the CaCl₂ doses (**Figure 6a,b**), but none of them exhibited dependence on shear zones (**Figure 6b**).

We then compared the fibrin formation between the non-treated and PMA-treated Vein-Chips. We longitudinally divided the CVS lumen by the central axis into the inner and

outer halves (**Figure 6c**). Intriguingly, while fibrin was mainly distributed at the inner wall without treatment (**Figure 6c**, upper), upon PMA stimulation, fibrin was deposited at both sides of the vessel wall (**Figure 6c**, lower). Compared to the non-treated condition (**Figure S3**, Supporting Information), the fibrin intensity at the outer half significantly increased by more than eight times upon PMA treatment (**Figure 6d**). For the non-treated condition, fibrin was expressed predominately at the inner half, with five times higher intensity relative to the outer half (**Figure 6d**).

2.6. Combine Virchow's Triad to Evaluate CVST on a Vein-Chip

Lastly, we combined all three thrombotic determinants on a CVS Vein-Chip with PMA-stimulated endothelium and hypercoagulable recalcified blood (**Figure 7a**). We first examined the hemodynamics with the fibrin expression. A significant similarity was observed between the fibrin deposition (**Figure 6a**; 3rd column, magenta) and the low shear pockets ($\gamma < 8$ s⁻¹) mapped by CFD analyses (**Figure 7b**, blue area). For further investigation, we drew three sample lines at each shear zone, and evenly selected five points at each sample line (**Figure 7b**; black crosses). On each point, CFD mapped shear

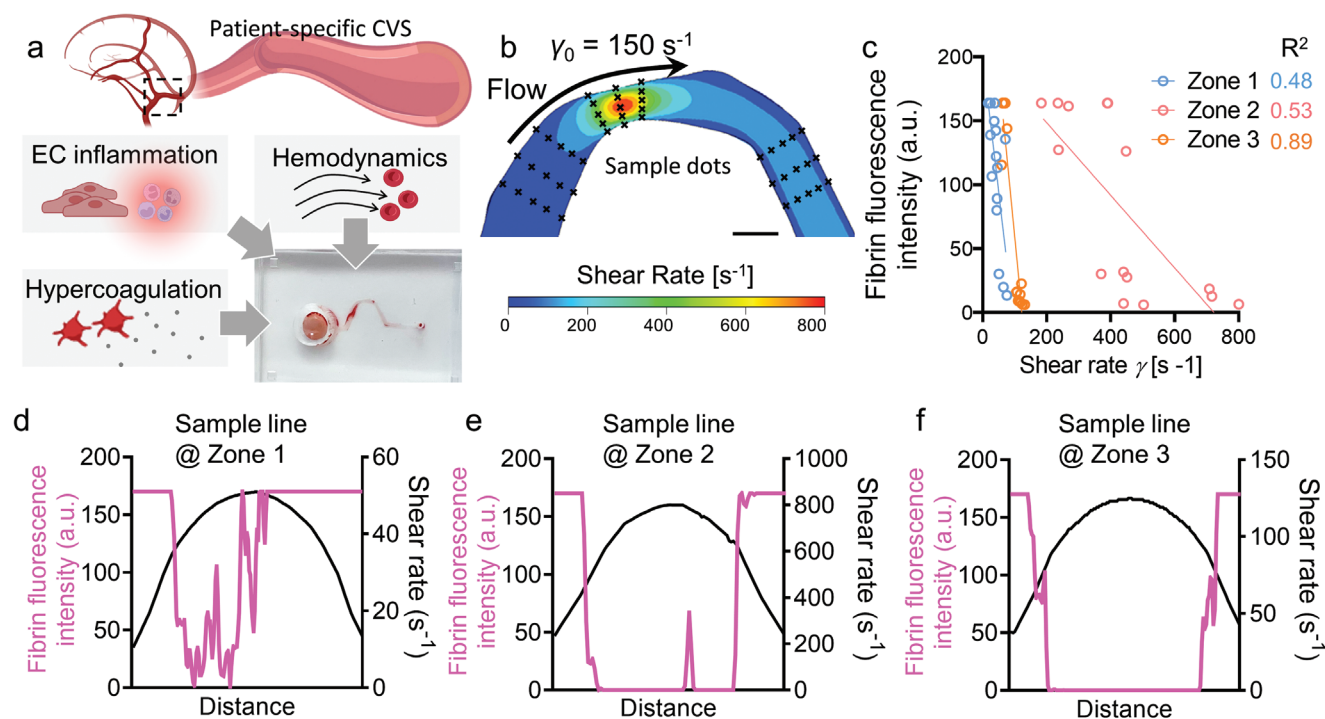


Figure 7. Combine Virchow's triad to evaluate CVST on a Vein-Chip. a) Illustration of Virchow's triad effects on the CVS Vein-Chip model and the representative photograph of fibrin-rich thrombi in a Vein-Chip after PFA fixation. b) CFD contour map showing shear rate distribution at the bottom of the Vein-Chip. Note that the low shear pockets mapped by the CFD contour map (blue area) are highly correlated with the fibrin deposition along the Vein-Chip in Figure 6a. Scale bar = 400 μm . c) Correlation of shear rate distribution and fibrin deposition across three rheological zones. Note that three lines and fifteen locations were sampled for correlation (crosses in b) for each zone. The fluorescence intensity of fibrin on a sample line (magenta) and the shear rate distribution at the same line (black) for zone 1 d), zone 2 e) and zone 3 f).

rate (Figure 7c) was correlated with fibrin fluorescent signals by confocal microscopy. Notably, zone 3 exhibited a strong correlation between fibrin intensity and shear rate, marked by a linear regression of $R^2 = 0.89$, confirming the post-stenosis low shear pocket favors coagulation. We then examined the fibrin fluorescence intensity at the middle sample lines of each zone, and compared it with the shear rate at the same lines. Zones 1 and 2 showed fluctuating fibrin intensity without a strong correlation to hemodynamic patterns (Figure 7d,e). However, zone 3 demonstrated an obvious negative correlations between fibrin intensity and shear rate (Figure 7f). Intriguingly, fibrin signals showed sudden drops when the shear rate reached 500 and 75 s^{-1} at zones 2 and 3, respectively (Figure 7e,f). Our data consistently showed that the fibrin formation is selectively deposited to the vessel wall, but not in the lumen (Figure 6), suggesting that fibrin formation requires a vessel wall and might also be relevant to platelet margination in whole blood perfusion.

Surprisingly, although the venous flow condition in our setup results in variations of the average shear rates across zones 1, 2, and 3, we did not observe a significant difference in terms of platelet and fibrin deposition. Nevertheless, it is reasonable to apply our approach to arterial vessels, and we may predict a more significant difference to arterial thrombosis, which is more sensitive to the shear threshold and flow patterns regulated by the systemic flow or vessel geometry.^[40,44]

3. Discussion

The innovation of this study introduced an affordable CVS-on-a-chip (Vein-Chip) that is a microfluidic model mimicking the venous geometry of a CVST patient, where living endothelial functionalization and whole blood perfusion recapitulates the patient-specific Virchow's triad—vessel wall morphology, hemodynamic flow disturbance, and coagulability. As a highlight, we reconstructed 3D CVS geometry from high-conventionally accepted method translated it into a Vein-Chip by 3D stereolithography. Moreover, to rapidly produce the industry-grade Vein-Chips in large quantities with various vascular geometries, we were inspired by the Chinese Type and invented a movable assembly system for low-cost mass production, with the ability to print multiple vascular segments simultaneously. Further, with localized shear mapping, the inclusion of the vascular endothelial function, and modulation of coagulability by recalcification, we systematically revealed the relative contribution of Virchow's triads to CVST on a chip in a personalized manner.

Despite the recent advances in clinical imaging modalities, thrombotic risk assessment still relies on invasive digital subtraction angiography. Although there are recent developments in 4D MRI and phase-contrast technologies, it is still not possible to accurately quantify Virchow's triad in the cerebral vasculature. Even worse, these facilities are only available in tertiary-level centers and are hard to access for most popula-

tions in underdeveloped regions. Besides the challenges in personalized diagnosis, antithrombotic treatment also lacks patient-specific assessment. Currently, there is no conventionally accepted method for testing the efficacy of antithrombotic therapy. This has led to significant stroke recurrence rates of up to 8.2% within the first 90 days, despite the implementation of intensive preventive strategies.^[45–47] As the first of its kind, our personalized CVS Vein-Chips bridge the gap between cerebrovascular imaging diagnostics and patient-specific blood clot testing. Our CVS Vein-Chips will not only provide more accurate diagnostic platforms, but also allow short- to long-term monitoring for cardiovascular patients with stroke, coronary artery stenosis, arteriovenous malformation, and aneurysm.

Numerous microfluidic and vessel-on-chip models have emerged to mimic vascular anatomies, incorporate hemodynamic parameters, and recapitulate platelet mechanobiology.^[25,36,48] These miniaturized microfluidic devices shed light on high-throughput,^[49,50] rapid and scalable blood clot testing,^[51,52] cerebral thrombosis diagnosis and prediction.^[5] Recent breakthroughs in 3D printing can potentially revolutionize the field of microfluidics by overcoming the limitations posed by conventional 2D wafer-based microfabrication techniques.^[41,53,54] Several studies have also examined progressive endothelial damage through physical techniques.^[55,56] For instance, optofluidic techniques have been demonstrated to elicit interactions with the vascular system.^[55] The CVS-on-a-chip proposed in this paper is anticipated to be utilized in further experiments incorporating regional physical stimulation on endothelial cells and creating a significant model for the study of vascular injury. With this technology, the blood vessel geometry can be printed as a chamber or rod. Nevertheless, there is still limited capacity for fabricating complex circular cross-section channels,^[25,48] let alone producing patient-specific 3D vasculature on a chip with low cost and fast turnover. To this end, our movable typed Vein-Chip fabrication solved such problems and can recapitulate the cerebral blood vessels containing U-shapes, bifurcations, and even more complex blood vessel networks. Besides, our methods overcame the bottleneck that comes with low-resolution 3D printers, which usually have a poor surface finish compared with silicon wafer-based lithography, resulting in leakage of the microfluidics and uneven focal plane during microscopy.

Last but not least, our movable typing enabled large-scale production of multiple blood vessel segmentations, thus significantly reducing fabrication time and cost. Specifically, the final products cost only \$5 for materials per chip and requires < 10 h fabrication time from a clinical image (Figure 2; Step 2: 1 h; Step 3: 4 h; Step 4: 2 h; Step 5: 2 h). These affordable chips enabled large-scale personalized thrombotic assessment from one to several at-risk patients for long-term monitoring at multiple time points. In an ideal future, our scaled-up, low-cost, and fast-turnover biofabrication capability by movable typing will not only provide a more accurate early prediction of thrombosis, but also enable personalized antithrombotic therapies. Future development of these personalized chips holds significant potential to help expand the Telehealth systems that link regional populations with central medical facilities and well-trained practitioners.

4. Experimental Section

MRV Image Acquisition: The MRV data of a patient were acquired with a dual-echo MRV pulse sequence on a Philips Medical Systems (Achieva) with a standard birdcage head coil. The standard consent procedure was followed. The readout bandwidth was equal to ± 15.6 kHz, and the flip angle was 20° . The matrix size for MRV data was $209 \times 239 \times 239$ ($k_x \times k_y \times k_z$), FOV = 240 mm, the slice thickness = 1.4 mm, the slice increment = 0.7 mm, 58.6% partial echo was used to decrease the TE1 of the first echo and maximize TE2 in the second echo.

Image reconstruction and post-processing were implemented in Mimics Research 21.0 with a personal computer (3.40 GHz CPU, 8 GB Memory). In order to suppress the serious artifacts caused by signal wrap-around along the slice direction, the reconstructed area was manually divided into vessel geometry used in this paper. A venogram was produced after implementing a minimum intensity projection (named as mIP to distinguish MIP) along the slice direction.

Printing and Material Selection: The vessel chip was manufactured using 3D stereolithography and soft lithography techniques (Figure S4, Supporting Information).

For the first step, the Standard Triangle Language (STL) file of blood vessel was extracted from the raw MRV images of the sigmoid sinus (Figure 2a). The image points were directly converted into STL format for digital reconstruction using a DICOM viewer.

For the second step, the STL file was converted into curvature-based continuous surfaces using the SpaceClaim software (ANSYS Inc. 2020) (Figure 2b). Manual adjustments in SpaceClaim were optional to modify the sharp edges and branches caused by image noise. The “smooth” function was then used to make a smooth vessel lumen, with the settings of “200% faces” and “60° angle” threshold. Finally, the “auto-skin” function generated the curvature-based continuous 3D vessel anatomy. In order to transfer the vessel geometry into a microfluidic device, the reconstructed sigmoid was first cut along the middle axial plane. Then a $30 \times 20 \times 6$ mm block was virtually created, followed by a Boolean subtraction to obtain the inner lumen of the vascular geometry (cf. Figure 2c).

From steps 3 to 5, several attempts were made to optimize each process. For the third step, a SLA 3D printer (Form 3B; FormLabs, Boston, USA) was utilized to fabricate a mold incorporating the vessel's details, using the “Clear V4” resin at a resolution of $25 \mu\text{m}$. A supportive structure was designed to increase the success rate and the z-direction precision (cf. Figure S1a, Supporting Information). The post-print treatment was performed using UV light oven produced by Formlabs under room temperature for 30 min (Video S1, Supporting Information). The principle for Step 3 of the manufacturing process was to choose an easily polished material. Two different resins, “Clear V4” and “Rigid 4K,” were utilized to print the negative mold. “Rigid 4K” offers superior mechanical properties, making it less susceptible to deformation. However, its opaque white color makes it challenging to inspect post-processing and it was discovered during experiments that the contact surface between other materials and “Rigid 4K” was difficult to cure, making it more challenging to create the intermediate positive mold.

“Clear V4” on the other hand, was transparent, and easier for visual inspection and diagnosis after post-processing. Additionally, the mold's transparency allows for the contact surface between the negative mold and other UV-cured material to be easily cured by applying UV light at the bottom of the mold when creating the intermediate positive mold. Furthermore, a thinner layer thickness of $\approx 25 \mu\text{m}$ could be achieved using “Clear V4” resin, which enabled the recovery of more vascular details. Therefore, “Clear V4” resin was selected to produce the negative mold.

For the fourth step, the major objective was to make the top surface mirror flat and smooth. To achieve this, a multi-staging polishing technique was used. In detail, the surface was first filed using 1200 grit sandpaper. To control the depth of filing, a rectangular trench with a controlled depth was designed in the printed mold. The desired depth was achieved when the trench started to vanish, and the first stage of polishing could stop. Then the 2500 grit sandpaper was used in the

second stage of polishing. The process was repeated until the grit number increased to 8000. Then the surface was polished to mirror smooth using an acrylic polish paste and a polishing cotton wheel. To control the flatness of the surface during polishing, another glass panel was placed underneath the sandpaper to ensure even contact between the surface and the sandpaper. The sandpaper was soaked in water to reduce the damage to the surface from the residual powder. After all the processes, the mold was washed in the ultrasonic cleaner to remove the jammed polishing paste inside the vessel and then dried with compressed air (Video S2, Supporting Information). At step 4, selecting the material for the intermediate positive mold was the most challenging aspect of the manufacturing process. First, the material must be fluid before curing to be poured into the negative mold. Second, the material must be soft after curing to be able to peel off from the solid negative mold. Lastly, the material must be able to separate from the PDMS for the final casting step. To meet these requirements, various materials were used to create the intermediate positive mold, including “Clear V4” resin, “Flexible” resin from Formlab, Loctite 385 UV cured epoxy, SU8 UV cured epoxy, and PDMS. The liquid “Clear V4” resin is too viscous to fill the entire negative mold, making it unable to recover all vessel details, and the cured part was filled with bubbles, rendering it unusable. Attempts using “Flexible” resin, Loctite 385, and SU8 UV cured epoxy also failed as it was difficult to peel off the cured mold from the negative mold, even after treating the negative mold with silane. Ultimately, PDMS was chosen as the material to produce the intermediate positive mold as it met all requirements and could be easily peeled off from the negative mold after silane treatment. After treating the PDMS intermediate positive mold with silane, it was possible to produce the negative PDMS vessel chip that met all requirements with a success rate greater than 90%.

Microfluidic Chip Fabrication: The polished chips from the last step were assembled into a large plate and treated with silane vapor (tridecafluoro 1,1,2,2-tetrahydrooctyle-1-trichlorosilane; Sigma-Aldrich). To fabricate the positive mold, polydimethylsiloxane (PDMS) (Sylgard 184 by Dow Corning) was mixed with the curing agent at a 10:1 ratio (w/w). Then the PDMS was poured on the assembled plate and heated in the oven at 60 °C for 4 h. After it was solidified, the cured PDMS was peeled off from the assembled plate and treated with silane vapor. To fabricate the microfluidic device, mixed PDMS was poured on the positive mold, and heated in the oven at 60 °C for 4 h. After it was solidified, the PDMS was peeled off from the positive mold and cut into pieces. Then the inlets and outlets of the PDMS chips were punched with Ø6 and Ø1 mm biopsy punchers (World Precision Instruments) for static and flow experiments, respectively. Lastly, the PDMS chip was permanently bonded to 0.17 mm glass slides after 3 mins plasma treatment for 3 min (Video S3, Supporting Information). In step 5, the selection principle was to find a biocompatible and transparent material. As PDMS has been widely accepted in the field and proven to be suitable for Lab-on-chip approaches, it was selected as the final microfluidic channel material.

Computational Fluid Dynamics Simulation: CFD simulation on the CVST geometry was performed using the commercially available ANSYS Fluent 2020 R1 software (version 20.1; Canonsburg, PA, USA) to map the flow field and calculate the shear rate in the domain. Given the abnormal shape of the cerebral venous sinus geometry, a tetrahedral dominant meshing method was selected with the maximum element size being 50 µm. A smooth transition inflation layer was applied to the entire body with the vessel walls acting as the boundary with the default transmission ratio used and growth rate of 1.1 with a maximum of 25 layers. Finally, edge sizing conditions were applied to have 50 elemental divisions for both left and right edges stemming from the inlets and outlets. The flow was assumed to be steady and laminar, and the fluid was considered Newtonian with constant properties. The flow rate was selected to be 81 µL min⁻¹ to achieve bulk shear rate $\dot{\gamma}_b = 150 \text{ s}^{-1}$. Finally, edge sizing conditions were applied to have 50 elemental divisions for both left and right edges stemming from the inlets and outlets.

Governing Equations and Numerical Formulation: Reynolds number (Re) was calculated to determine if the flow was laminar or turbulent:

$$\text{Re} = \frac{\rho Q D_h}{\mu A} \quad (1)$$

where ρ and μ denote the density and viscosity of the fluid, respectively. Q is the outflow rate, D_h and A are the hydraulic diameter and surface area of the cross-section of the domain, respectively. As a result, the Re numbers were 140.9 for the MRV scale vessel geometry and 1.32 for the microfluidic scale channel, indicating that the flow was laminar for both cases. Following the laminar assumption of flow and considering the fluid as Newtonian with constant properties, the continuity equation, and the well-known Navier Stokes equations can be used for computational fluid dynamics simulation:

$$\nabla \cdot u = 0 \quad (2)$$

$$\rho(u \cdot \nabla u) = -\nabla P + \mu \nabla^2 u \quad (3)$$

where u is the 3D velocity vector, ρ is the density, P is the pressure, and τ is the shear stress term. For the boundary conditions, a mass-flow outlet, a zero-gauge pressure inlet, and a non-slip wall were applied in CFD to comply with the experiments.

Endothelialization of CVST Chips: Human umbilical endothelial cells (HUVECs) were obtained from Thermo Fisher Scientific and cultured with EGM-2 medium (EGM-2 BulletKit, Lonza). Once reached 80–90% confluency, HUVECs (passages 3–7) were washed with phosphate-buffered saline (PBS, ThermoFisher) and trypsinized using trypsin/EDTA solution (ThermoFisher). After centrifuge, HUVECs were resuspended in EGM-2 medium at a seeding density of $\approx 5 \times 10^6 \text{ cells mL}^{-1}$. Prior to HUVECs seeding, the microfluidic chip was sterilized with 80% ethanol for 20 min and washed three times with PBS. Then the microfluidic channels were coated with 100 µg mL⁻¹ human plasma fibronectin (Thermo Fisher) and incubated at 37 °C for one hour. The channels were then rinsed with PBS twice, and then 8 µL of prepared HUVECs suspension was injected from the outlet into the microchannel. The microfluidic chip was then immediately flipped upside down to allow HUVECs attachment to the dome of the microchannel for 15 min. Then the chip was flipped again to allow HUVECs to attach to the bottom surface for 20 min. After that, the EGM-2 medium was added to the inlet reservoir to culture HUVECs statically overnight, and the endothelialization of the microfluidic chip was completed.

In the study of the effect of endothelial cell inflammation on platelet and fibrin deposition, the microvessels were activated with phorbol myristate acetate (PMA, 50 ng mL⁻¹ in serum-free medium EBM-2) for 1.5 h at static conditions. Then the microvessels were washed with complete medium EGM-2 twice. Then the microvessels were ready for further examination.

Microfluidic Chip Immunofluorescence Staining: Proceeding PMA treatment, devices were fixed with 4% formaldehyde solution, followed by a 1 h blocking period in 5% Bovine Serum Albumin (BSA) in PBS. The microfluidic chips were then incubated with a primary antibody solution containing 2% BSA overnight at 4 °C. Afterwards, secondary antibodies were delivered at room temperature for 1–2 h in 2% BSA/PBS, followed by nuclei staining for 10 min in PBS alone.

E-selectin (CD62E) immunofluorescence was performed using a primary mouse anti-human monoclonal antibody (CL2; dilution 1:200, eBioscience) and polyclonal, Alexa Fluor 555 conjugated donkey anti-mouse secondary (dilution 1:500, Invitrogen). ICAM-1 (CD54) staining was performed using Alexa Fluor 488 conjugated anti-human ICAM-1 (HA58; dilution 1:200, Stock In-House). Nuclei were stained using Hoechst33342 (dilution 1:4000, Invitrogen) for cell identification within the channel.

Immunofluorescence images of local zones 1, 2, and 3 were taken using Olympus confocal microscope FV3000, and z-projections were obtained using max intensity projection on ImageJ software. Signal overlaps between channels were removed using ImageJ's LUMos Spectral Unmixer Plugin (<https://imagej.net/plugins/lumos-spectral-unmixing>)

with 1 fluorophore, 50 replicates, and 100 iterations. Individual channels were then converted to an 8 bit binary scale and measured for their mean grey value using a randomized Region of Interest (ROI) ImageJ macro with more than 50 regions for each image in both non-treated and PMA-treated conditions.

Blood Collection: All procedures involving blood collection from healthy donors were approved by the University of Sydney Human Research Ethics Committee (HREC, project 2014/244). All human donor blood samples were obtained with written informed consent. Blood was collected from healthy donors with written informed consent and anticoagulated in 3.2% sodium citrate vacutainers (Becton Dickinson) or preloaded syringe tubes as previously described.^[24,58,59]

Whole Blood Perfusion and Imaging Procedure: Whole blood was stained for platelets with anti-CD41-Atto555 (SZ22) (0.5 $\mu\text{L mL}^{-1}$) and fibrin with anti-fibrin (0.5 $\mu\text{L mL}^{-1}$). The anti-CD41 antibody was from Beckman Coulter. The Fibrin antibody 59D8 was from Freda Passam, labeled with AlexaFluor 594 using protein labeling kit A10239 (Invitrogen). Currently, there are no standardized recalcification concentrations or methods for microfluidic assays to evaluate the circulating physiology and hypercoagulation Ca^{2+} levels that allow for reproducible thrombi generation across in vitro assays. Here, the whole blood perfusion protocol was optimized on the Vein-Chip to model thrombosis by performing a recalcification titration in the citrated blood and modeling the coagulability. Blood was collected from healthy donors and labeled with platelets and fibrin markers.

After staining, whole blood was recalcified in 1 mL aliquots immediately before use in the assay with one in 100 dilutions of the relevant concentration of CaCl_2 to achieve the desired concentration. Blood was introduced at the channel inlet of the PDMS block, which was cut into a 200 μL reservoir. The flow was induced with a 2 mL syringe connected to the outlet, withdrawn by a PHD ULTRA pump (Harvard Apparatus). Platelet aggregation, fibrin expression, and EC presentation were monitored with combined three-color confocal microscopy with concurrent DIC imaging (Olympus FV3000RS confocal microscope with a $\times 30$ silicon oil objective). Fluorescent images were captured using FLUOVIEW software, version 2.6 (Olympus). Blood flow was observed within a focal plane $\approx 30 \mu\text{m}$ above the coverslip bottom of the channels. Fluorescently labeled platelet aggregates were quantitatively analyzed on a frame-by-frame basis offline using IMARIS (Bitplane AG, Oxford Instruments).

To examine the endothelial and thrombosis biomarkers, the Vein-Chip was fixed with 4% paraformaldehyde after blood perfusion, and then thoroughly washed with PBS. Subsequently, the Vein-Chip was imaged using an Olympus FV3000RS confocal microscope and operated by FLUOVIEW software.

Endothelial Cell Morphology Quantification: To quantify the influence of PMA on the endothelium, the circularity of the endothelial cell body, the F-actin positive area, and the F-actin length were calculated. The circularity of the endothelial cell body was automatically calculated by IMARIS (Bitplane AG, Oxford Instruments) using the cell segmentation technique. The circularity of a cell was defined by the ratio of the cell surface area of a sphere (with the same volume as the given particle) to the cell surface area of the particle (Wadell 1932). To compare the influences of PMA treatment on F-actin, the F-actin positive area was calculated, defined as the percentage of the area of the single cell F-actin, with an intensity value over 650 measured by ImageJ, to the area of a cell body ($n \geq 30$). Then the length of the F-actin in a single cell was manually measured. The histogram graphs are plotted in Figure 4d–f.

Statistical Analysis: All graphical data were presented by GraphPad Prism 9.0. Statistical differences between each group were tested by the unpaired, two-tailed Student's *t*-test. A *p*-value below 0.05 was accepted as significant.

Ethics Statement: The clinical imaging protocol is simplified and uniform for all patients assessed for possible acute stroke. All patients underwent MRV, irrespective of the duration of symptoms at the time of assessment. The research protocol was approved by the Prince of Wales Hospital Human Research Ethics Committee. Data will be made

available upon reasonable request. The data are not publicly available due to privacy or ethical restrictions.

Supporting Information

Supporting Information is available from the Wiley Online Library or from the author.

Acknowledgements

The authors thank Drs Zhiyong Li, Ken Butcher, Leon Edwards, and James McFadyen for helpful discussion on clinical imaging and thrombosis diagnosis. The authors thank Shaun Jackson and HRI Thrombosis Group for blood sample collection support. The authors thank Gemma Figtree and Clare Arnott for clinical guidance and support. The authors thank Hongxu Lu and Guocheng Fang for providing critical suggestions. This work was supported by the Australian Research Council (ARC) (DP200101970 – L.A.J.); the National Health and Medical Research Council (NHMRC) of Australia (APP2003904 – L.A.J.; GNT2022247 – Y.C.Z.); NSW Cardiovascular Capacity Building Program (Early-Mid Career Researcher Grant – L.A.J.); MRFF Cardiovascular Health Mission Grants (APP2016165 – L.A.J.; APP2023977 – L.A.J., T.A., F.P., and A.C.); Ramaciotti Foundations (2020HIG76 – L.A.J.); National Heart Foundation (106979 – L.A.J.; 106879 – Y.C.Z.), Office of Global and Research Engagement (International Sustainable Development Goal Program – L.A.J.), and Sydney Nano Research Schemes (Grand Challenge – L.A.J.). L.A.J. is a National Heart Foundation Future Leader Fellow Level 2 (105863). All experiments were performed in accordance with relevant guidelines and approved by the University of Sydney Human Research Ethics Committee. Informed consent were obtained from human participants of this study. All data that support the findings of this study are available on request from the corresponding author.

Open access publishing facilitated by The University of Sydney, as part of the Wiley - The University of Sydney agreement via the Council of Australian University Librarians.

Conflict of Interest

The authors declare that they have a patent related to the technology described in this article. The potential conflict of interest has been disclosed and managed in accordance with the journal's policy on declaration of conflicting interest.

Author Contributions

L.A.J. and Y.C.Z. wrote and revised the paper, performed research and analyzed data, conducted analysis and interpretation of data, and designed research. Y.Z., S.A., and Y.W. cultured the endothelial cells, functionalized the chips, and treated them with PMA in the microfluidic devices. Y.Z., S.A., and A.N. performed immunostaining. A.S. and L.M. assisted in blood sample collection. T.A. provided the MRV images and contributed the preliminary data. Z.W. performed the stereolithography and polished the chips. F.J. wrote and revised the manuscript and performed analysis and interpretation of the data. K.K. and P.V. assisted with the computational fluid dynamics simulation and microfluidic designs. S.A., T.H., P.V., A.C., Q.P.S., and F.P. co-wrote and revised the final manuscript.

Data Availability Statement

The data that support the findings of this study are available from the corresponding author upon reasonable request.

Keywords

biofabrications, fibrin, mechanobiology, organ on chips, shear stress, strokes, thrombosis

Received: December 5, 2022

Revised: February 3, 2023

Published online: March 28, 2023

- [1] V. L. Feigin, B. A. Stark, C. O. Johnson, G. A. Roth, C. Bisignano, G. G. Abady, M. Abbasifard, M. Abbasi-Kangevari, F. Abd-Allah, V. Abedi, A. Abualhasan, N. M. Abu-Rmeileh, A. I. Abushouk, O. M. Adebayo, G. Agarwal, P. Agasthi, B. O. Ahinkorah, S. Ahmad, S. Ahmadi, Y. A. Salih, B. Aji, S. Akbarpour, R. O. Akinyemi, H. Al Hamad, F. Alahdab, S. M. Alif, V. Alipour, S. M. Aljunid, S. Almustanyir, R. M. Al-Raddadi, et al., *Lancet Neurol.* **2021**, *20*, 795.
- [2] Y. S. Zhang, F. Davoudi, P. Walch, A. Manbachi, X. Luo, V. Dell'Erba, A. K. Miri, H. Albadawi, A. Arneri, X. Li, X. Wang, M. R. Dokmeci, A. Khademhosseini, R. Oklu, *Lab Chip* **2016**, *16*, 4097.
- [3] Y. Zhang, F. Jiang, Y. Chen, L. A. Ju, *Front. Pharmacol.* **2021**, *12*, 779753.
- [4] D. L. Bark, A. N. Para, D. N. Ku, *Biotechnol. Bioeng.* **2012**, *109*, 2642.
- [5] Y. Qiu, B. Ahn, Y. Sakurai, C. E. Hansen, R. Tran, P. N. Mimche, R. G. Mannino, J. C. Ciciliano, T. J. Lamb, C. H. Joiner, S. F. Ofori-Acquah, W. A. Lam, *Nat. Biomed. Eng.* **2018**, *2*, 453.
- [6] J. M. Ferro, P. Canhão, J. Stam, M.-G. Bousser, F. Barinagarrementeria, *Stroke* **2004**, *35*, 664.
- [7] P. Digge, K. Prakashini, K. V. Bharath, *Indian J. Radiol. Imaging* **2018**, *28*, 280.
- [8] A. R. Bateman, G. A. Bateman, T. Barber, *Fluids Barriers CNS* **2021**, *18*, 5.
- [9] J. M. Coutinho, J. M. Ferro, P. Canhão, F. Barinagarrementeria, C. Cantú, M.-G. Bousser, J. Stam, *Stroke* **2009**, *40*, 2356.
- [10] D. A. de Sousa, P. Canhão, I. Crassard, J. Coutinho, A. Arauz, A. Conforto, Y. Béjot, M. Giroud, J. M. Ferro, *Stroke* **2017**, *48*, 3130.
- [11] C. de Gregorio, G. Calcaterra, N. G. Kounis, P. P. Bassareo, J. L. Mehta, *Lancet Reg. Health: Eur.* **2022**, *16*, 100387.
- [12] L. PalaioDIMOU, M.-I. Stefanou, A. H. Katsanos, D. A. de Sousa, J. M. Coutinho, P. Lagiou, I. Michopoulos, A. Naska, S. Giannopoulos, K. Vadikolias, K. I. Voumvourakis, V. Papaevangelou, T. I. Vassilakopoulos, S. Tsiodras, G. Tsvigoulis, *Neurology* **2021**, *97*, e2136.
- [13] Stroke Foundation. Clinical Guidelines for Stroke Management 2017, Melbourne Australia.
- [14] L. Saba, T. Saam, H. R. Jäger, C. Yuan, T. S. Hatsukami, D. Saloner, B. A. Wasserman, L. H. Bonati, M. Wintermark, *Lancet Neurol.* **2019**, *18*, 559.
- [15] N. Khandelwal, A. Agarwal, R. Kochhar, J. R. Bapuraj, P. Singh, S. Prabhakar, S. Suri, *AJR, Am. J. Roentgenol.* **2006**, *187*, 1637.
- [16] H. H. Hu, C. R. Haider, N. G. Campeau, J. Huston, S. J. Riederer, *J. Magn. Reson. Imaging* **2008**, *27*, 653.
- [17] G. J. del Zoppo, *Rev. Neurol. Dis.* **2008**, *5*, S12.
- [18] A. Kopczak, A. Schindler, D. Sepp, A. Bayer-Karpinska, R. Malik, M. L. Koch, J. Zeller, C. Strecker, D. Janowitz, F. A. Wollenweber, J.-M. Hempel, T. Boeckh-Behrens, C. C. Cyran, A. Helck, A. Harloff, U. Ziemann, S. Poli, H. Poppert, T. Saam, M. Dichgans, *J. Am. Coll. Cardiol.* **2022**, *79*, 2189.
- [19] B. Fuentes, R. Gutierrez-Zuniga, E. Diez-Tejedor, *Front. Neurol.* **2020**, *11*, 653.
- [20] O. Miraucourt, S. Salmon, M. Szopos, M. Thiriet, *Comput. Methods Biomech. Biomed. Eng.* **2017**, *20*, 471.
- [21] C. M. Wu, K. McLaughlin, D. L. Lorenzetti, M. D. Hill, B. J. Manns, W. A. Ghali, *Arch. Intern. Med.* **2007**, *167*, 2417.
- [22] M. F. Giles, P. M. Rothwell, *Lancet Neurol.* **2007**, *6*, 1063.
- [23] A. J. Coull, J. K. Lovett, P. M. Rothwell, *BMJ* **2004**, *328*, 326.
- [24] Y. Chen, L. A. Ju, F. Zhou, J. Liao, L. Xue, Q. P. Su, D. Jin, Y. Yuan, H. Lu, S. P. Jackson, C. Zhu, *Nat. Mater.* **2019**, *18*, 760.
- [25] L. A. Ju, S. Kossmann, Y. C. Zhao, L. Moldovan, Y. Zhang, S. De Zoysa Ramasundara, F. Zhou, H. Lu, I. Alwis, S. M. Schoenwaelder, Y. Yuan, S. P. Jackson, *Analyst* **2022**, *147*, 1222.
- [26] G. Feher, D. Hargroves, Z. Illes, P. Klivenyi, L. Liu, L. Szapary, *Front. Neurol.* **2021**, *12*, 762060.
- [27] Y. Zhuo, J. Wu, Y. Qu, H. Yu, X. Huang, B. Zee, J. Lee, Z. Yang, *Medicine* **2020**, *99*, e20830.
- [28] H. Ay, L. Gungor, E. M. Arsava, J. Rosand, M. Vangel, T. Benner, L. H. Schwamm, K. L. Furie, W. J. Koroshetz, A. G. Sorensen, *Neurology* **2010**, *74*, 128.
- [29] D. Chaudhary, V. Abedi, J. Li, C. M. Schirmer, C. J. Griessenauer, R. Zand, *Front. Neurol.* **2019**, *10*, 1106.
- [30] M. Bussotti, H. Qi, *East Asian Sci. Technol. Med.* **2014**, *40*, 9.
- [31] D. J. Lee, A. Ahmadpour, T. Binyamin, B. C. Dahlin, K. Shahlaie, B. Waldau, *J. Neurointerv. Surg.* **2017**, *9*, 34.
- [32] Y. C. Zhao, Y. Zhang, F. Jiang, C. Wu, B. Wan, R. Syeda, Q. Li, B. Shen, L. A. Ju, *Adv. Healthcare Mater.* **2022**, *12*, e2201830.
- [33] A. Volkov in *Encyclopedia of Membranes* (Eds: E. Drioli, L. Giorno), Springer, Heidelberg, Germany **2015**, pp. 1–2.
- [34] C. Guttridge, A. Shannon, A. O'Sullivan, K. J. O'Sullivan, L. W. O'Sullivan, *Ann. 3D Printed Med.* **2022**, *5*, 100044.
- [35] B. Shen, A. Tasdogan, J. M. Ubellacker, J. Zhang, E. D. Nosyreva, L. Du, M. M. Murphy, S. Hu, Y. Yi, N. Kara, X. Liu, S. Guela, Y. Jia, V. Ramesh, C. Embree, E. C. Mitchell, Y. C. Zhao, L. A. Ju, Z. Hu, G. M. Crane, Z. Zhao, R. Syeda, S. J. Morrison, *Nature* **2021**, *591*, 438.
- [36] Y. C. Zhao, P. Vatanekah, T. Goh, R. Michelis, K. Kyanian, Y. Zhang, Z. Li, L. A. Ju, *Sci. Rep.* **2021**, *11*, 6875.
- [37] K. J. van Stralen, F. R. Rosendaal, C. J. Doggen, *Arch. Intern. Med.* **2008**, *168*, 21.
- [38] M. H. Meissner, T. W. Wakefield, E. Ascher, J. A. Caprini, A. J. Comerota, B. Eklof, D. L. Gillespie, L. J. Greenfield, A. R. He, P. K. Henke, A. Hingorani, R. D. Hull, C. M. Kessler, R. D. McBane, R. McLafferty, *J. Vasc. Surg.* **2007**, *46*, S25.
- [39] A. Dupuy, L. Hagimola, N. S. A. Mgaith, C. B. Houlahan, R. E. Preketes-Tardiani, P. R. Coleman, F. H. Passam, *Diagnostics* **2021**, *11*, 203.
- [40] N. K. Rajeeva Pandian, B. K. Walther, R. Suresh, J. P. Cooke, A. Jain, *Small* **2020**, *16*, 2003401.
- [41] N. V. Menon, C. Su, K. T. Pang, Z. J. Phua, H. M. Tay, R. Dalan, X. Wang, K. H. H. Li, H. W. Hou, *Biofabrication* **2020**, *12*, 045009.
- [42] A. Jain, A. Graveline, A. Waterhouse, A. Vernet, R. Flaumenhaft, D. E. Ingber, *Nat. Commun.* **2016**, *7*, 10176.
- [43] E. Westein, A. D. van der Meer, M. J. E. Kuijpers, J.-P. Frimat, A. van den Berg, J. W. M. Heemskerk, *Proc. Natl. Acad. Sci. USA* **2013**, *110*, 1357.
- [44] A. V. Belyaev, M. A. Panteleev, F. I. Ataullakhanov, *Biophys. J.* **2015**, *109*, 450.
- [45] Y. Wang, Y. Wang, X. Zhao, L. Liu, D. Wang, C. Wang, C. Wang, H. Li, X. Meng, L. Cui, J. Jia, Q. Dong, A. Xu, J. Zeng, Y. Li, Z. Wang, H. Xia, S. C. Johnston, *N. Engl. J. Med.* **2013**, *369*, 11.
- [46] S. C. Johnston, P. Amarenco, G. W. Albers, H. Denison, J. D. Easton, S. R. Evans, P. Held, J. Jonasson, K. Minematsu, C. A. Molina, Y. Wang, K. S. L. Wong, *N. Engl. J. Med.* **2016**, *375*, 35.
- [47] S. C. Johnston, P. Amarenco, H. Denison, S. R. Evans, A. Himmelmann, S. James, M. Knutsson, P. Ladenvall, C. A. Molina, Y. Wang, *N. Engl. J. Med.* **2020**, *383*, 207.
- [48] Y. C. Zhao, H. Wang, Y. Wang, J. Lou, L. A. Ju, *RSC Chem. Biol.* **2022**, *3*, 707.

- [49] L. H. Ting, S. Feghhi, N. Taparia, A. O. Smith, A. Karchin, E. Lim, A. St. John, X. Wang, T. Rue, N. J. White, N. J. Sniadecki, *Nat. Commun.* **2019**, *10*, 1204.
- [50] P. Guruprasad, R. G. Mannino, C. Caruso, H. Zhang, C. D. Josephson, J. D. Roback, W. A. Lam, *Am. J. Hematol.* **2019**, *94*, 189.
- [51] C. E. Hansen, W. A. Lam, *Anal. Chem.* **2017**, *89*, 11881.
- [52] S. Satta, A. Lai, S. Cavallero, C. Williamson, J. Chen, A. M. Blázquez-Medela, M. Roustaei, B. J. Dillon, N. Ashammakhi, D. D. Carlo, Z. Li, R. Sun, T. K. Hsiai, *Adv. Sci.* **2021**, *8*, e2103266.
- [53] P. F. Costa, H. J. Albers, J. E. A. Linssen, H. H. T. Middelkamp, L. van der Hout, R. Passier, A. van den Berg, J. Malda, A. D. van der Meer, *Lab Chip* **2017**, *17*, 2785.
- [54] N. V. Menon, H. M. Tay, S. N. Wee, K. H. H. Li, H. W. Hou, *Lab Chip* **2017**, *17*, 2960.
- [55] L. Chen, Y. Zheng, Y. Liu, P. Tian, L. Yu, L. Bai, F. Zhou, Y. Yang, Y. Cheng, F. Wang, L. Zheng, F. Jiang, Y. Zhu, *Lab Chip* **2022**, *22*, 1344.
- [56] L. Chen, L. Yu, Y. Liu, L. Bai, F. Wang, Y. Zhu, *Cell Rep. Med.* **2022**, *3*, 100765.
- [57] C. Provost, M. Soudant, L. Legrand, W. Ben Hassen, Y. Xie, S. Soize, R. Bourcier, J. Benzakoun, M. Edjlali, G. Boulouis, H. Raoult, F. Guillemin, O. Naggara, S. Bracard, C. Oppenheim, **(2019)**, Magnetic Resonance Imaging or Computed Tomography Before Treatment in Acute Ischemic Stroke. *Stroke*, *50*(3), 659–664, <https://doi.org/10.1161/strokeaha.118.023882>.
- [58] A. Dupuy, L. Hagimola, N. S. A. Mgaïeth, C. B. Houlahan, R. E. Preketes-Tardiani, P. R. Coleman, F. H. Passam, **(2021)**, Thromboinflammation Model-on-A-Chip by Whole Blood Microfluidics on Fixed Human Endothelium. *Diagnostics*, *11*(2), 203, <https://doi.org/10.3390/diagnostics11020203>.
- [59] L. Ju, J. D. McFadyen, S. Al-Daher, I. Alwis, Y. Chen, L. L. Tønnesen, S. Maiocchi, B. Coulter, A. C. Calkin, E. I. Felner, N. Cohen, Y. Yuan, S. M. Schoenwaelder, M. E. Cooper, C. Zhu, S. P. Jackson, **(2018)**, Compression force sensing regulates integrin $\alpha 1 \text{b} \beta 3$ adhesive function on diabetic platelets. *Nature Communications*, *9*(1). <https://doi.org/10.1038/s41467-018-03430-6>.